A finite volume local defect correction method for solving the transport equation

A finite volume local defect correction method for solving the transport equation

W. Kramer [a,c,*], R. Minero [b,c], H. J. H. Clercx [a,c,d] and R. M. M. Mattheij [b,c]

[a] *Fluid Dynamics Laboratory, Department of Applied Physics, Eindhoven University of Technology, P.O. Box 513, 5600 MB Eindhoven, The Netherlands*

[b] *Department of Mathematics and Computer Science, Eindhoven University of Technology, The Netherlands*

[c] *J.M. Burgers Centre, Research School for Fluid Dynamics*

[d] *Department of Applied Mathematics, The Netherlands University of Twente, The Netherlands*

Abstract

The local defect correction (LDC) method is applied in combination with standard finite volume discretizations to solve the advection-diffusion equation for a passive tracer. The solution is computed on a composite grid, *i.e.* a union of a global coarse grid and local fine grids. For the test a dipole colliding with a no-slip wall is used to provide an actively changing velocity field. The LDC method is tested for the problem of localized patch of tracer material that is transported by the provided velocity field. The LDC algorithm can be formulated to conserve the total amount of tracer material. However, if the local fine grids are moved to adaptively follow the behaviour of the solution, a loss or gain in the total amount of tracer material is produced. This deficit in tracer material is created when the solution is interpolated to obtain data for the moved fine grid. The data obtained by the interpolation scheme in the new refined region can be adapted in such a way that the deficit is spread over the new grid points and conservation of tracer material is satisfied. Finally, the results of the conservative finite volume LDC method are compared and validated with results from a spectral method.

Key words: local defect correction, finite volume methods, grid refinement, transport equation, spectral methods
PACS: 47.11.Df, 47.11.Kb, 47.11.St

* w.kramer@tue.nl

1 Introduction

Transport of passive tracers is modelled by an advection-diffusion equation, and it has been studied from both a phenomenological and an experimental point of view by many authors, see review articles [1; 2; 3] and references therein. In turbulent flows, one of the main difficulties to solve advection-diffusion problems from a computational point of view is the scale separation between main flow eddies and transport processes: the latter occur usually at a scale which can be considerably smaller than the smallest length scales of the turbulent flow [1]. Considering the fact that running direct numerical simulations (DNS) of the main flow is already challenging for simple geometries, but still feasible using for example spectral methods, we see that it is much more difficult to properly simulate the transport processes. In practical applications, the tracer material might be confined to a very limited part of the computational domain, so that dedicated numerical tools cas solve the problem. Other examples of solutions of partial differential equations (PDEs) exhibiting local regions of high activity are frequently encountered also in many other areas, like shock hydrodynamics, combustion, etc.

An efficient numerical solution of problems with highly localized properties can be computed using adaptive grid techniques. In adaptive grid methods, a fine grid spacing and possibly a small time step are adopted only where the large variations occur, so that the computational effort and the memory requirements are minimized. A large number of adaptive grid methods for time-dependent problems have been proposed in the literature. A first category includes the moving-grid or dynamic-regridding methods. In this approach, nodes are moving continuously in the space-time domain, like in classical Lagrangian methods, and the discretization of the PDEs is coupled with the motion of the grid. The grid is anyhow always nonuniform and the number of nodes remains constant in time. The nonuniformity of the grid implies that programming these methods often involves quite complicated data structures. Another type of adaptive grid techniques is represented by static-regridding methods. Here, the idea is to adapt the grid at each time step by adding grid points where a high activity occurs and removing them where they are no longer needed. This process is controlled by error estimates or by measures of some characteristics of the solution (e.g. gradients, slope, etc.). In this kind of methods the number of grid points is not constant in time.

An example of a static-regridding technique is the local uniform grid refinement (LUGR) method, described and analyzed in Refs. [4; 5; 6]. The method works as follows: at each time step the PDE is first integrated on a global uniform coarse grid. The coarse grid solution at the new time step provides artificial boundary conditions on a local uniform fine grid and the problem is then solved locally with a smaller time step than the one used on the global

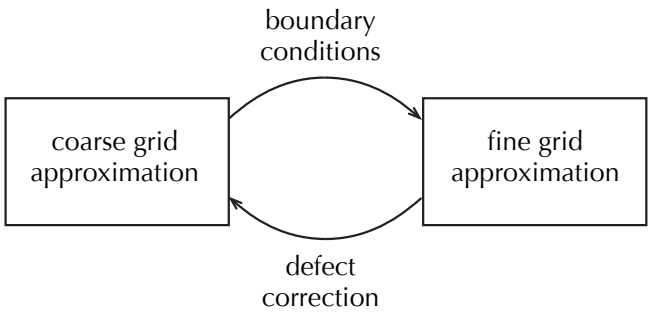

Fig. 1. The local defect correction algorithm solves the global coarse grid and local fine grid separately. The coarse grid solution provides boundary conditions for the fine grid problem. The fine grid solution is used to correct the defect in the coarse grid solution.

grid. At this point, the fine grid values are used to replace the coarse grid values in the region of refinement. The technique relies on the fact that the coarse grid solution provides artificial boundary conditions for the local problem that are accurate enough. This article focuses on another static-regridding technique for time-dependent problems: local defect correction (LDC). LDC for time-dependent problems has been introduced in [7]. LDC shares with LUGR the possibility and the advantage of working with uniform grids and uniform grid solvers only. In LDC, however, the fine grid solution at the new time step is used not only to replace the coarse grid values in the area of refinement, but to overall improve the coarse grid approximation. This can be achieved through a defect correction, in which the fine grid solution is used to approximate the coarse grid local discretization error. The improved coarse grid approximation defines new artificial boundary conditions for a new local problem, which in turn can correct the solution globally. In this way, LDC does not have to rely on the accuracy of the artificial boundary condition provided by the first coarse grid approximation. The LDC algorithm is schematically represented in figure 1.

In Ref. [8] LDC is coupled with standard finite volume discretizations and an algorithm can be formulated in such a way that on the composite grid the solution is conservative. When the fine grid is fixed, conservation of tracer material has been verified in practise using a simple prescribed velocity field. If the local fine grid moves in time to cover the change of the solution in time, interpolating the solution is necessary to obtain data on the new fine grid. The interpolation introduces a deficit in tracer material, and therefore the LDC algorithm in total is then not conservative. In this paper we test the LDC method as described in [7] for a more realistic flow. Direct numerical simulations of dipolar vortex colliding with a no-slip wall are used to provide an actively changing velocity field. The transport of a small patch of tracer material, located near the point of impact of the dipole with the no-slip boundary, is then computed using the LDC method. For this case we investi-

gate the impact of the deficit in tracer material introduced by the regridding, and introduce a conservative regridding strategy to obtain an overall better conservative scheme. Finally, we compare the results of the LDC method to the data obtained with a spectral method.

This paper is structured in the following way. First, in sections 2 and 3 we give a description of the finite volume LDC method. For a more detailed description of the finite volume LDC method the reader is referred to [7]. The test problem and the settings used to solve the velocity field and tracer distribution are introduced in section 4. The velocity field corresponding to the dipole-wall collision process is obtained by a spectral simulation, and the tracer dispersion is resolved using the finite volume LDC method. In section 5 we investigate the conservation of tracer material by the LDC method, and more specifically, the mass deficit introduced during the regridding stage. The conservative regridding strategy is discussed in section 6, where also its conservative properties are verified. Finally, we compare the results, obtained using the conservative LDC method in combination with the new regridding scheme, to the results from a spectral computation.

2 A finite volume local defect correction method

The dispersion of a passive tracer with a diffusion coefficient κ in a given velocity field $\mathbf{u}$, is governed by an advection-diffusion equation. In integral formulation for a volume V, the advection-diffusion equation for the tracer concentration $c(t, \mathbf{x})$ reads

$$\frac{\partial}{\partial t} \int_V c dA + \int_{\partial V} \mathbf{f} \cdot \mathbf{n} ds = 0 \quad \text{in } \Omega, \tag{1}$$

where the flux vector is given by $\mathbf{f} = c\mathbf{u} - \kappa \nabla c$ and $\mathbf{n}$ is the outward pointing unit vector normal to the boundary ∂V. We use a global spatial grid Ω^H with a grid size H_x and H_y on which we want to find an approximation $c^H(\mathbf{x}_{ij})$ for the concentration. The grid points are given by $\mathbf{x}_{ij} = (x_i, y_j) = (iH_x, jH_y)$ where i and j are integer numbers. In order to apply (1), we divide the domain in a number of control volumes $V_{ij} = (x_{i-1/2}, x_{i+1/2}) \times (y_{j-1/2}, y_{j+1/2})$ as is illustrated in figure 2. The size of the control volumes $H_x \times H_y$ determines the spatial accuracy of the finite volume method. The total amount of tracer material in the control volume follows from $T_{ij} = \int_{V_{ij}} c dA$. In the absence of a tracer source the only cause for an increase of the amount of tracer material are the tracer fluxes across the boundaries of the control volume, ∂V_{ij}. The integral flux across the upper boundary of the control volume is given by

$$F_{i,j+1/2}(c) = \int_{x_{i-1/2}}^{x_{i+1/2}} \mathbf{f}(s, y_{i,j+1/2}) \cdot \mathbf{n} ds. \tag{2}$$

The fluxes across the other three boundaries of the control volume are governed by similar expressions. If (1) is applied to a control volume we obtain,

$$\frac{\partial}{\partial t} T_{ij}(c) + [\Sigma^H F(c)]_{ij} = 0, \tag{3}$$

where the operator $[\Sigma^H F(c)]_{ij}$ denotes the sum over the integral fluxes across all four boundaries of the control volume.

The integrals T and F must be numerically approximated by a quadrature rule and a suitable choice is the midpoint rule. For example, the midpoint rule applied to T yields $T_{ij} \approx c(\mathbf{x}_{ij}) H_x H_y$. We provide the approximations for both integrals with the superscript H, *i.e.* T^H and F^H, respectively. These particular choices for the integral approximations will result in a grid as is depicted in figure 2, where values for the concentration c^H are specified at the centres of the control volume $\mathbf{x}_{ij}$ and the integrated fluxes F^H are calculated at the midpoints of the boundaries. To calculate F^H the flux f of (2) at the midpoints of the boundaries are evaluated using second-order central-differences.

In addition to the spatial discretization (3) still needs to be discretized in time in order to be used numerically. Therefore, we introduce $t^n = n\Delta t$, where n is an integer number and Δt a discrete time step. If we apply the implicit Euler scheme and insert the approximations T^H and F^H in (3), we obtain

$$T_{ij}^H(c^{H,n}) - T_{ij}^H(c^{H,n-1}) + \Delta t \Sigma_{ij}^H [F^H(c^{H,n})] = 0, \tag{4}$$

with $c^{H,n} = c^H(t^n)$. The implicit Euler scheme is here used for its clear notation. The local defect correction algorithm does not specifically require the implicit Euler scheme, the use of other implicit time schemes is also appropriate.

The global domain Ω is divided into a integer number of control volumes to construct the coarse grid denoted by Ω^H. To proceed in time from t^{n-1} to t^n we can straightforwardly apply (4) when the concentration $c^{H,n-1}$ is known and the boundary conditions are specified.

In a local region of the domain, denoted by Ω_l, the solution exhibits small-scale structures and thus requires a higher spatial and time resolution. Now we want to compute a local solution $c_l^{h,n}$ on Ω_l at t^n with a better spatial and time accuracy, which is then used to improve the coarse grid solution $c^{H,n}$. To compute a more accurate local fine solution we introduce a local finer grid Ω_l^h, which consists of control volumes with a smaller size $h_x \times h_y$. For the application of LDC it is convenient to let the boundaries of the coarse grid control volumes coincide with the boundaries of the fine grid control volumes. In order to have the coarse grid points inside the refinement area to coincide with points of the fine grid, we choose the refinement factors $\sigma_x = H_x/h_x$ and

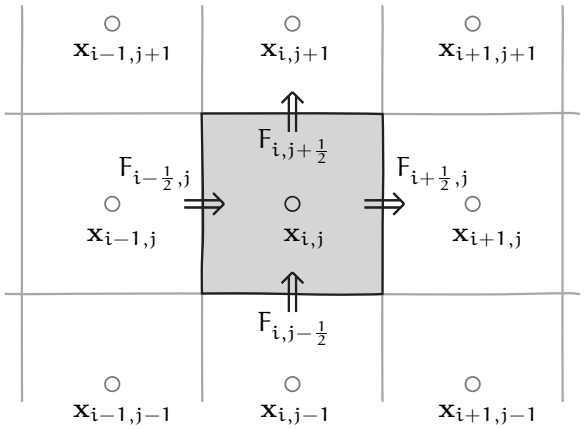

Fig. 2. Grid for the finite volume approach, the circles give the interior grid points $x_{i,j}$ at the centre of the control volumes $V_{i,j}$, the fluxes are calculated on the interfaces between two control volumes.

$\sigma_y = H_y/h_y$ to be odd integers. The centres of the small control volume, *i.e.* the grid points of the fine grid Ω_l^h, are given by $(x_{i+p/\sigma_x}, y_{j+q/\sigma_y})$ with

$$p = -(\sigma_x - 1)/2, -(\sigma_x - 3)/2, \ldots, (\sigma_x - 1)/2, \tag{5}$$
$$q = -(\sigma_y - 1)/2, -(\sigma_y - 3)/2, \ldots, (\sigma_y - 1)/2. \tag{6}$$

An example of a fine grid with the refinement factors $\sigma_x = \sigma_y = 3$ is provided in figure 3. In order to solve the local problem we need to specify boundary conditions on the interface between the local fine grid and the coarse grid. The concentration in the fine grid points on the interface, that do not coincide with coarse grid points, can be obtained using a spatial interpolation scheme.

Since in the local region the solution exhibits high activity, not only the grid size but also the time step required for solving the fine grid problem δt might be smaller than the time step used for the global grid problem. One time step for the global time step is divided in τ smaller time steps. The fine grid problem than needs to be solved for the intermediate time levels $t_{n-1+k/\tau}$ with $k = 1, \ldots, \tau$. The solution is obtained by applying the same finite volume method (4) as is used for the global problem. To provide the values for the concentration on the interface between the coarse and global grid as required to specify the boundary conditions for the local problem, we need to interpolate the coarse grid solution in time. If the fine grid boundary $\partial\Omega_l$ coincides with the global boundary, a physical boundary condition (in our case, no-flux) can applied. Now the boundary values for the concentration $c_l^{h,n-1+k/\tau}$ for the refined area are known, the solution on the interior fine grid points can be computed.

With both the coarse grid solution $c^{H,n}$ and fine grid solution $c^{h,n}$ known at

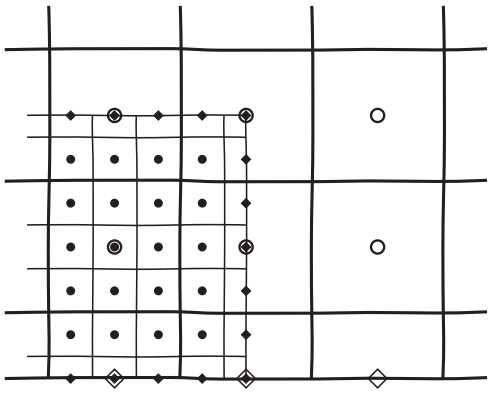

Fig. 3. Grid composed of the coarse grid and the fine grid, where the refinement factor is three for both directions. Open circles and diamonds give the interior and boundary grid points on the global grid Ω^H, respectively. Closed circles represent the grid points of the fine grid Ω_l^h, while closed diamonds are the grid points at the interface between the fine and coarse grid.

t^n we define the composite solution as

$$c^{H,h,n} = \begin{cases} c_l^{h,n} & \text{on } \Omega_l^h \\ c^{H,n} & \text{on } \Omega^{H,h} \setminus \Omega_l \end{cases} \tag{7}$$

The composite grid $\Omega^{H,h}$ is the union of the coarse grid Ω^H and the fine grid Ω^h. If the exact continuous solution $c(t)$ is known, we would be able to calculate the defect of the finite volume discretization. This is done by inserting the exact solution $c^n = c(t_n)$ in the discretized equation (4), yielding

$$d_{ij}^n = T_{ij}^H(c^n) - T_{ij}^H(c^{n-1}) + \Delta t[\Sigma^H F^H(c^n)]_{ij}, \tag{8}$$

for all coarse grid points. The defect can then be used to correct the coarse grid solution by adding the defect d^n to the right-hand side of (4), where it acts like a source term.

As we do not know the exact solution the composite solution $c^{H,h,n}$ is used to find an approximation for the defect,

$$d^{H,n} = T^H(c^{H,h,n}) - T^H(c^{H,h,n-1}) + \Delta t \Sigma^H F^H(c^{H,h,n}). \tag{9}$$

To calculate the defect at the coarse grid points outside the refinement area, only the coarse grid solution is available. As the coarse grid solution satisfies (4), the defect outside the refinement area Ω_l is equal to zero.

The approximate defect (9) is then used to correct the global coarse grid solution. Now, we need to recalculate the fine grid solution once more, but with new boundary values provided by the new coarse grid solution. These

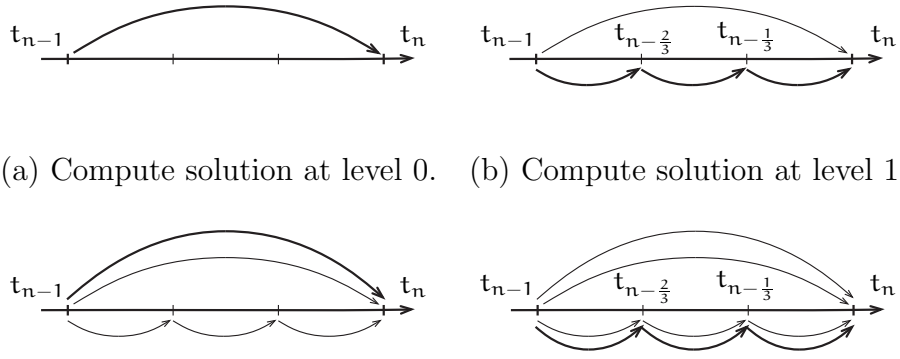

(a) Compute solution at level 0. (b) Compute solution at level 1.

(c) Correct solution at level 0. (d) Update solution at level 1.

Fig. 4. The local defect correction method with different time steps used to solve the coarse and fine grid problems. In this example one coarse grid time step Δt is divided in three smaller time steps δt used to obtain the fine grid solution.

steps can be repeated to obtain an even better solution, but in practise one LDC iteration is sufficient to obtain an accurate solution [9].

The time stepping process is schematically represented in figure 4. First one big time step Δt is made to obtain the c_H on t_n. To obtain the fine grid solution at t_n we need to make τ smaller time steps for the fine grid problem. Boundary conditions for the fine grid problem on the intermediate time levels are provided by interpolating the coarse grid solution in time and space. The fine grid solutions are used to calculate a defect for the coarse grid problem. Now, we solve the coarse grid problem with the corrected source term to obtain c^H at t_n. Finally, we recompute the fine grid solutions at all the intermediate times with updated boundary conditions and arrive with c^h also at t_n.

With the defect defined in (9) the LDC algorithm functions properly, but conservation of tracer material is not ensured. During one time step Δt, nothing guarantees that the coarse and fine tracer fluxes are in balance across the interface between the coarse and the fine grid.

3 The finite volume adapted defect term

To make the finite volume LDC algorithm conservative [8], a slightly different definition for the defect is used. The idea is to write the defect term in such a way that the balance of fluxes across the interface is guaranteed during every time step. Therefore, we return to the exact equation (3), which is valid for a

control volume V_{ij}. Integrating this equation between t_{n-1} and t_n yields

$$T(c^n) - T(c^{n-1}) + \Sigma^H \int_{t_{n-1}}^{t_n} F(c)dt = 0. \tag{10}$$

Note that the T and F represent the exact integrals and not the approximations. Relation (10) is subtracted from the defect definition (9),

$$\begin{aligned} d^n =& [T^H(c^n) - T(c^n)] - [T^H(c^{n-1}) - T(c^{n-1})] \\ &+ \Sigma^H [F^H(c^n)\Delta t - \int_{t_{n-1}}^{t_n} F(c)dt]. \end{aligned} \tag{11}$$

To obtain a value for the defect we have to approximate the integrals $T(c^n) = \int_{V_{ij}} c^n dA$ and $\mathcal{F}(c^n) = \int_{t_{n-1}}^{t_n} F(c)dt$. Approximations are made by using the best data available, *i.e.* the fine grid solution if available and the coarse grid solution otherwise. A summation over the tracer material in the fine grid control volumes

$$T^{\text{sum}}_{l,ij} = \sum_{p=-(\sigma_x-1)/2}^{(\sigma_x+1)/2} \sum_{q=-(\sigma_y-1)/2}^{(\sigma_y+1)/2} T^h_{l,i+p/\sigma_x,j+q/\sigma_y}(c^{h,n}) \tag{12}$$

will result in the approximation for $T(c^n)$. If no fine solution is available the best approximation that can be found is $T^H(c^{H,h,n})$. Thus we have

$$T(c^n) \approx T^{\text{best}}(c^{H,h,n}) = \begin{cases} T^{\text{sum}}_l(c^{h,n}_l) & \text{on } \Omega^h_l \\ T^H(c^{H,h,n}) & \text{on } \Omega^{H,h} \setminus \Omega_l. \end{cases} \tag{13}$$

In figure 5 both cases are graphically represented if the integral $T(c^n) = \int_{V_{ij}} c^n dA$ is calculated using the midpoint rule. Applying the midpoint rule to a coarse grid control volume is analog to saying that $c^{H,h,n}$ is constant in the control volume, which is represented by the single colour. The best estimation than is $T^{\text{best}} = T^H = c^{H,n} H_x H_y$. On the fine grid the midpoint rule is applied to the fine grid control volumes, $T^h_l = c^{h,n}_l h_x h_y$. For the best approximation all these fine grid contributions T^h_l are summed to find $T^{\text{best}}(c^{H,h,n})$ for a coarse control volume.

The time integral over the integrated fluxes in (11),

$$\mathcal{F}^n_{i+1/2,j} = \int_{t_{n-1}}^{t_n} F_{i+1/2,j}(c)dt, \tag{14}$$

needs some more consideration as we have a solution on the fine grid with both a better spatial and a better time accuracy. For finding an approximation for the integrand we define

$$F^{\text{sum}}_{l,i+1/2,j}(c^h_l(t)) = \sum_{q=-(\sigma_y-1)/2}^{(\sigma_y-1)/2} F^h_{l,i+1/2,j+q/\sigma_y}(c^h_l(t)). \tag{15}$$

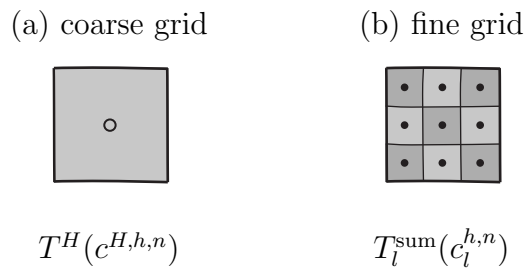

Fig. 5. The best approximation for $T(c^n) = \int_{V_{ij}} c^n dA$ is found (a) using the c^H on the coarse grid or (b) by summing over all fine grid contributions.

The integral over time in (14) can be best approximated using the fine grid solution at all the intermediate time levels $t_{n-1+k/\tau}$. The best approximation is thus obtained by summing the fine grid fluxes, $F_l^h(c_l^{h,n-1+k/\tau})$, over all fine control volumes within the coarse control volume and over all intermediate time levels. If only the coarse grid solution is available, the best approximations for $\mathcal{F}^n_{i+1/2,j}$ is simply $F^H_{i+1/2,j}(c^{H,h,n})\Delta t$. Summarizing, the approximation of $\mathcal{F}^n$ is given by

$$\mathcal{F}^n \approx \mathcal{F}^{\text{best}}(c^{H,h,n}) = \begin{cases} \sum_{k=1}^{\tau} F_l^{\text{sum}}(c^{h,n-1+k/\tau})\delta t & \text{on } \Omega_l^h \\ F^H(c^{H,h,n})\Delta t & \text{on } \Omega^{H,h} \setminus \Omega_l \end{cases} \tag{16}$$

In figure 6 we illustrate this for the fluxes through the right boundary of the coarse grid control volume. The single coarse grid flux, denoted by the arrow, is the only available approximation for $\int_{t_{n-1}}^{t_n} F(c)dt$ on the coarse grid. If a fine grid solution is available, the best approximation follows from a summation over all fine grid fluxes at all intermediate time levels.

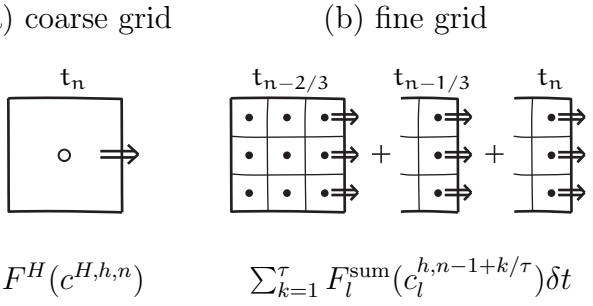

Fig. 6. Finding the best approximation for $\int_{t_{n-1}}^{t_n} F(c)dt$ using (a) the single flux on the coarse grid solution or (b) the fluxes at in the fine control volumes at $t^{n-1+k/\tau}$ with $k = 1, \ldots, \tau$. The relevant fluxes for calculating $\mathcal{F}^n_{i+1/2,j}$ are denoted by the arrows.

To approximate the discretization error we substitute the exact solution c^n with the composite solution $c^{H,h,n}$ in equation (11). If we insert the approximations for the integrals (13) and (16), the approximate adapted defect is

given by,

$$d^{H,n} = [T^H(c^{H,h,n}) - T^{\text{best}}(c^{H,h,n})] - [T^H(c^{H,h,n-1}) - T^{\text{best}}(c^{H,h,n-1})] + \Sigma^H[F^H(c^{H,h,n})\Delta t - \mathcal{F}^{\text{best}}(c^{H,h,n})]. \quad (17)$$

Outside the refinement area all the best approximation for the integrals are given by the coarse grid versions and hence the adapted effect is here zero. For all coarse grid points inside the refinement area the adapted defect is equal to the standard defect (9), as the contributions of T^{best} and $\mathcal{F}^{\text{best}}$ cancel each other[8]. The difference between using the standard definition for the defect or the adapted definition stems from the defect calculated on the coarse grid point that lie on the interface between coarse and fine grid. Such a grid cell is given in figure 7. For these points we cannot use the fine grid solution to find approximations for $T_{ij}(c^n)$ as it only covers a part of the coarse grid control volume, thus we have to fall back on the coarse grid solution and use $T^{\text{best}}(c^{H,h,n}) = T^H(c^{H,h,n})$. The same is valid when approximating the fluxes on this grid cell, one side (a) of the coarse control volume is not covered by the fine grid and two sides (b) are only partially covered by the fine grid. Here, the relation $\mathcal{F}^{\text{best}}(c^{H,h,n}) = F^H(c^{H,h,n})\Delta t$ must be used when calculating the defect. The only exception is the side of the control volume (c) that lays completely in the refinement area, and thus the fine grid fluxes can be used. The defect calculated for points that lay on the interface reduces to

$$d_{ij}^{H,n} = F_{ij}^H \Delta t - \sum_{k=1}^{\tau} F_l^{\text{sum}}(c_l^{h,n-1+k/\tau})\delta t. \quad (18)$$

If the LDC iteration is converged, *i.e.* the defect $d_{ij}^{H,n}$ goes to zero, the coarse grid flux $F_{ij}\Delta t$ is matched by the sum over the fine grid fluxes. Now, the amount of tracer that flows across the interface during one time step Δt is equal for the coarse grid solution and for the fine grid solution. Therefore, using the adapted definition of the defect (11) the total amount of tracer material is conserved. Mathematical proof that conservation of tracer material is ensured when the adapted defect is used, is given in Ref. [8]).

4 Tracer transport by a dipole-wall collision as a test problem

The dipole-wall collision (for example, see Refs. [10; 11]) is used as a way to provide a dynamic time-dependent velocity field to the transport equation (see figure 8). A dipole with symmetric vorticity cores translates along a straight trajectory. It can be orientated in a direction that leads towards a wall with the no-slip boundary condition. At the no-slip walls viscous boundary layers are created to satisfy the no-slip boundary condition. When the vortex cores of the dipole are close to the wall, boundary layer vorticity is detached from the

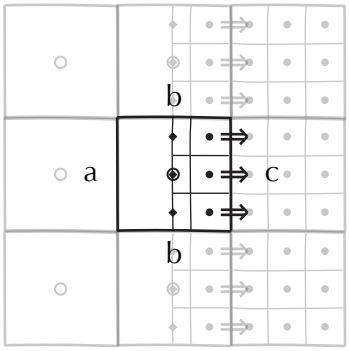

Fig. 7. A grid cell that lies on the interface between the coarse and the fine grid. Only the fine grid fluxes indicated by the arrows can be used to find the an approximation for $\int_{t_{n-1}}^{t_n} F(c)dt$.

wall. The detached boundary layer vorticity then rolls up forming secondary vortices. This set-up is proposed as a benchmark problem for two-dimensional Navier-Stokes solvers [12]. The strong interaction between the dipole and the viscous boundary layer leads to the formation of strong gradients in the velocity field. The Navier-Stokes equation is solved by a pseudo-spectral method using $N = 128$ Fourier and $M = 128$ Chebyshev polynomials. The viscosity, ν, is chosen to be relatively large, which yields a moderate initial Reynolds number, $\mathrm{Re} = 250$. This done to obtain a well-resolved velocity field. The Reynolds number, given by $\mathrm{Re} = u_{\mathrm{rms}}L/\nu$, is based on the r.m.s. velocity and the half height of the channel, which are both equal to one for the initial condition. The time step, $\Delta t_{\mathrm{flow}} = 1.25 \times 10^{-5}$, for solving the Navier-Stokes equation is of the same order as the smallest time step used to solve the transport equation with the LDC finite volume method or the pseudo-spectral method. The Adams-Bashforth/Crank-Nicolson time discretization scheme is used, which will provide accurate results due to the small time step. The settings for the simulations are summarized in table 1.

In this velocity field we place a blob of tracer material close to the boundary, where the dipole will impinge. The tracer diffusion is set to $\kappa = 2 \times 10^{-3}$ resulting in an initial Péclet number of $\mathrm{Pe} = 500$. The Péclet number, given by $\mathrm{Pe} = UL/\kappa$, is based using the r.m.s. velocity and the half height of the domain. At the lower and upper boundary the no-flux conditions are applied for the tracer concentration. The blob with tracer will be stretched and deformed during the collision of the dipole with the wall yielding steep gradients in the concentration. For the initial tracer field a Gaussian distribution is used

$$c(t = 0, \mathbf{x}) = \frac{1}{2\pi\sigma^2} \exp(-|\mathbf{r}|^2/2\sigma^2), \tag{19}$$

where $\mathbf{r} = \mathbf{x} - \mathbf{x}_0$ with $\mathbf{x}_0$ the centre of the blob. The centre of the blob is placed at $\mathbf{x}_0 = (1, -1)$, *i.e.* at the wall. The variance is chosen to be small, $\sigma = \sqrt{2}/20$, so the distribution of tracer material is confined to a small local

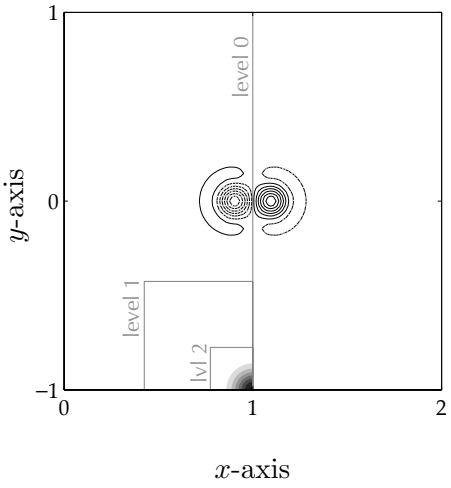

Fig. 8. The initial conditions for the test problem. The initial vorticity field is indicated by the contours and the initial tracer distribution is represented by the different levels of grey. The coarse global grid for the LDC method covers the left half of the domain $[0, 1] \times [-1, 1]$. The two refined grids are given by the squares.

area. The total amount of tracer material located in the Gaussian blob is equal to one. In our case the centre of the blob is located at the wall $y = -1$, thus only half of the material is situated inside the domain. As most of the dynamics in the flow field appear to occur close to the boundary, the centre of

Table 1
Settings of the simulations for benchmarking the finite volume local defect correction method. The velocity field needed is solved with a spectral method

- velocity field -

ν	Re	N	M	Δt
4×10^{-3}	250	128	128	1.25×10^{-5}

- tracer field - spectral

κ	Pe	N_t	M_t	Δt
2×10^{-3}	500	768	768	1.25×10^{-5}

- tracer field - LDC

κ	Pe	level	$1/H_x$	$1/H_y$	$\Delta t_{\max}$	$\Delta t_{\min}$
2×10^{-3}	500	0	20	20	1.0×10^{-3}	2.0×10^{-4}
		1	100	100	2.0×10^{-4}	4.0×10^{-5}
		2	500	500	4.0×10^{-5}	0.8×10^{-5}

the tracer blob is placed at the crossing of the dipole axis and the boundary $(x_c, y_c) = (1, -1)$. Note that this set-up results in a symmetrical evolution of the tracer relative to $x = 1$. For the finite volume LDC method, we exploit this symmetry by computing the solution only on half the domain, namely the left part $[0, 1] \times [-1, 1]$. Along the symmetry line $x = 1$ a no-flux boundary condition is applied.

For testing the local defect correction method a standard finite volume method is used, in which the fluxes and integrals are approximated using the second order central-difference formula and the midpoint rule, respectively. For this case two levels of refinement are applied, where the global grid size $H_x = H_y = 1/20$ and the refinement factor is equal to $\sigma_x = \sigma_y = 5$, at both levels. The velocity data is provided by the pseudo-spectral method on the 128×128 grid with a nonuniform grid point distribution. As different grids are used by the spectral method and the LDC method, piecewise linear spatial interpolation is used to obtain data that can be used by the finite volume method on the various grid levels. The time step used is also not necessarily the same for both methods. When no velocity field is present at the current time, the data are obtained by piecewise linear time interpolation. The boundary values for the fine grid problems are found by applying piecewise quadratic interpolation at both refinement levels. The time-discretization in the LDC method is performed by the first order backward Euler scheme at grid levels 0 (global) and 1, and by the θ-method for the grid level 2 (finest). Setting $\theta = 0.51$ yields a second order accurate scheme with better damping properties than the Crank-Nicolson scheme ($\theta = 0.5$). The time step for the global grid is adaptive within the range $[1 \times 10^{-3}, 2 \times 10^{-4}]$ and for grid levels 1 and 2 the time refinement factor is $\tau = 5$. The control parameter δ_∞ for determining the time step is based on the maximum change in the concentration on the coarse grid

$$\delta_\infty = \Delta t \left|\left| c^{H,h,n-1}|_{\Omega^H} - c^{H,h,n-2}|_{\Omega^H} \right|\right|_\infty. \tag{20}$$

If the value for δ_∞ is within the preset range $[6 \times 10^{-6}, 1 \times 10^{-5}]$, the time step is not altered. But if δ_∞ exceeds one of the limits, the time step is changed accordingly to get the control parameter back in the desired range. The actual time step used during the simulation is given in figure 9.

To compute the composite solution at t_n, the solutions on all the three levels needs to progress to the new time. Adding another level of refinement (level 2) with an even smaller time step can increase the complexity enormously. However, we can reduce the complexity and consequently the amount of work required to compute the solution by making some assumptions. We briefly describe the time stepping strategy with two levels of refinement, a more detailed description is given in ref. [13]. Initially we proceed as described in section 2 for the two level system. After we have computed the level 0 solution with the corrected source term, *i.e.* after step (c) in figure 4, we can provide boundary conditions to the level 1 problem at all intermediate times. Now, we assume

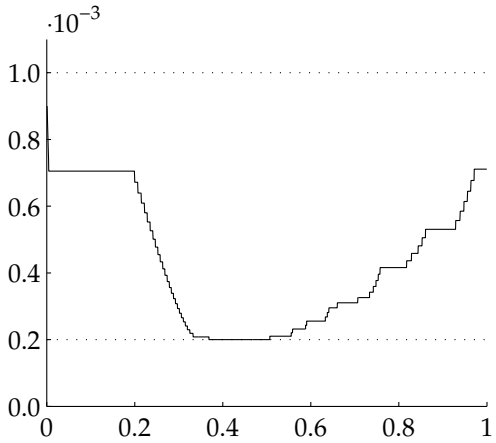

Fig. 9. The time step Δt used for solving the transport equation is adapted during the LDC simulations within the range $[\Delta t_{\min}, \Delta t_{\max}]$.

that the high activity in the solution, which does require the finest level of grid refinement, does not influence the global solution at the interface between the level 0 and level 1 grids. Thus the boundary conditions for the level 1 problem do not depend on the level 2 solution. With these boundary conditions fixed we can use the basic two-level LDC time stepping, where level 1 is the coarse grid and level 2 takes the place on the fine grid. Because we use smaller time steps on the level 1 grid than on the coarse grid we have to apply the basic two-level LDC time stepping τ times to arrive with the level 1 and 2 solutions at t_n. In total the global solution has to be computed twice, the level 1 solutions have to be computed three times and the solutions on the finest grid has to be computed twice.

5 Numerical results for the LDC finite volume method

The results obtained with the LDC finite volume method are presented in figure 10. In the first stage the dipole and the blob of tracer material are far apart and hence the tracer distribution does not change much. When the dipole reaches the wall at $t \approx 0.4$ some part of the tracer distribution is squeezed between the wall and the dipole. This results in very strong gradients in the concentration close to the wall. The other part of the tracer blob is advected around the dipole cores, as a result the tracer material is injected into the interior of the domain. Note that the level 2 grid is also elongated to cope with this advection of the tracer material. The repositioning of the refined grids is done automatically, based on a detection algorithm for regions with high activity [14; 15; 16]. As the dipole cores start to separate from each other along the wall ($t \approx 0.6$), tracer material is transported away from the symmetry line. With no tracer material left at the symmetry line there is no need for a fine grid.

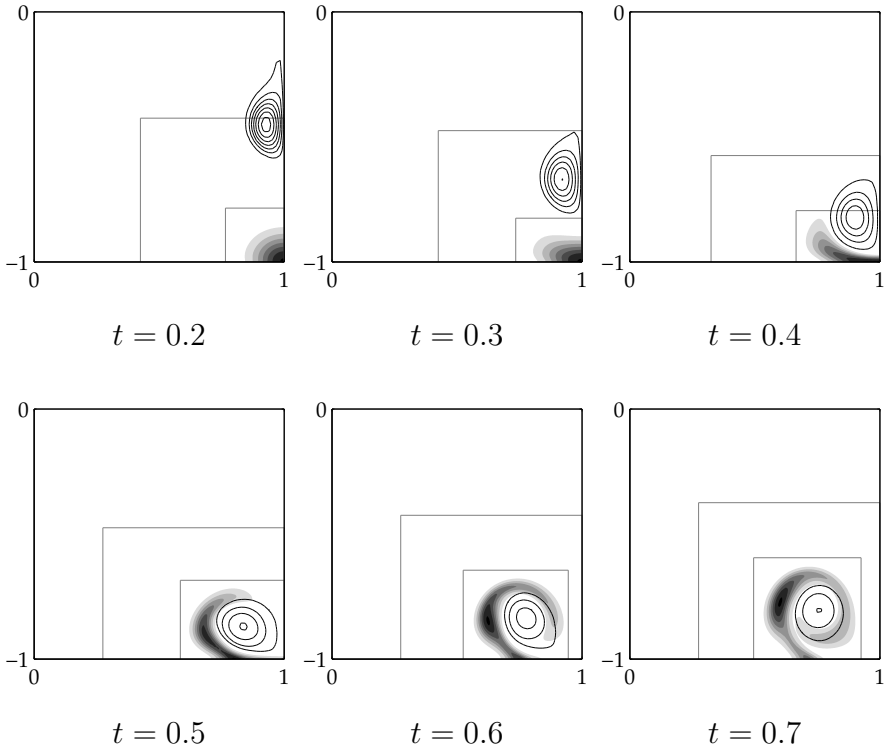

Fig. 10. Simulation results of the LDC finite volume method for the advection of tracer distribution during a dipole-wall collision. The lower left quarter of the entire domain $[0, 2) \times [-1, 1]$ is visible. The dipole is visualized by the vorticity contours, for visibility only negative contours are plotted. The tracer concentration are represented by the grey levels, black for maximum concentration and white for zero concentration. The grey rectangles give the locations of the local domains for the two refinement levels.

Now we compare the dynamic adjustment of the time step method to the evolution of the tracer material. In the early stages $t = 0 - 0.2$ when the change in the tracer distribution is small the used time step on the global grid is large $\Delta t = 7 \times 10^{-4}$. When the dipole is closing in on the wall and the tracer, the time step is rapidly decreased until the minimum is reached at $t \approx 0.4$. Thereafter, the time step is steadily increasing as the tracer is advected around one dipole core and gradients in the tracer distribution are decreased in magnitude by diffusion. Adapting the time step reduces the total number of steps required for the simulation approximately with a factor two.

After the formulation of a conservative version of the LDC finite volume method in section 3 it is interesting to see how well the LDC method reproduces the conservation law. As we apply no-flux boundary conditions on the global domain and there is no source of tracer material, the total amount of tracer material,

$$M(t) = \int_{\Omega} c(t, \mathbf{x}) dA, \tag{21}$$

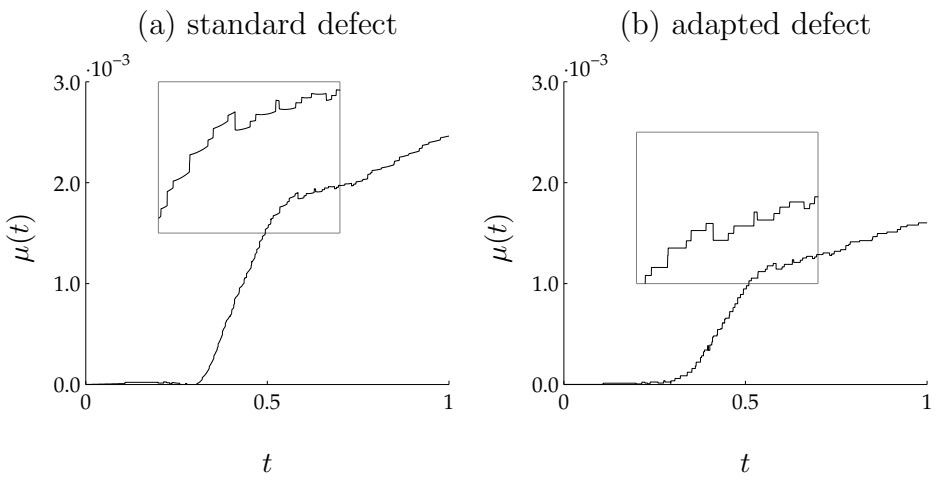

Fig. 11. The relative error $\mu(t)$ in the total amount of tracer material obtained with (a) the standard defect (9) and (b) the adapted finite volume defect (11). The inset gives a zoomed view for the time interval [0.5,0.7].

is fixed to its initial value. In the LDC method the integral is computed using the best data, *i.e.* the fine solutions if available and otherwise the coarse solution. The relative change in total amount of tracer material $\mu(t) = (M(t) - M(0))/M(0)$ is given in figure 11 for both the standard defect (9) and the adapted defect (11). The LDC method based on the standard choice for calculating the defect (9), the total amount of tracer material changes in time. While using the adapted finite volume defect (11) improves conservation properties we still see some increase of total amount of tracer material. The cause for this becomes clear if we zoom in on the curve to the level where separate time steps are visible. For the standard defect the total amount of tracer material changes during each time step, which can be expected as the method is not conservative. However the change seems to be more abrupt for some time levels. These abrupt changes coincide with the times the fine grid changes. The curve for the adapted finite volume defect shows the same abrupt changes, but between the regridding the scheme is conservative. Until now we did not speak about how to handle movement of the grid as it is not inherent to the LDC mechanism. Regridding in a conservative way is a broader problem, which we aim to address next.

6 Conservative regridding

In the previous section we have seen that while the adapted LDC finite volume is conservative there is quite some increase of total amount of tracer material due to the movement of the fine grid. The high activity in the solution moves and changes its size as time proceeds. Consequently, the local grid $\Omega_l^{h,n}$ used to perform the time step from t_{n-1} to t_n might not fully cover the high activity

region during the next time step. The new local fine grid $\Omega_l^{h,n+1}$ used to compute the solution at t_{n+1} has to be moved and reshaped to capture the high activity in the solution. As data from the previous time level t_n is required on the new grid for the next time step, an approximation $c_*^{H,h,n}$ must be found at all the points of the new composite grid $\Omega^{H,h,n+1}$. With the solution at t_n computed on the old composite grid $\Omega^{H,h,n}$, the fine grid approximation of c^n is only available in the common grid points of the old fine grid $\Omega_l^{h,n}$ and the new fine grid $\Omega_l^{h,n+1}$. On the remaining part of $\Omega^{H,h,n+1}$ a solution has to be computed via interpolation from $c^{H,h,n}$. Thus the approximation $c_*^{H,h,n}$ is given by

$$c_*^{H,h,n} = \begin{cases} Q_x^n(c^{H,h,n}) \text{ on } \Omega_l^{h,n+1} \\ c^{H,h,n} \qquad \text{on } \Omega_l^{H,h,n+1} \setminus \Omega_l^{h,n+1}. \end{cases} \tag{22}$$

where Q_x^n denotes a spatial interpolation operator that has been used in the earlier mentioned simulations. Here, the operator Q_x^n performed piecewise quadratic interpolation. But as noted before this regridding leads to an increase of the total amount of tracer material, a side effect which is not desired. Changing to higher order interpolation methods did not results in a better conservation of tracer material.

In order to obtain a way to make the regridding conservative, we can separate two different causes for the change in the amount of tracer material. The first occurs for the coarse grid points that lay inside the refinement area at t_n but do not at t_{n+1}, *i.e.* the course grid points included in $\Omega_l^{H,h,n+1} \setminus \Omega_l^{h,n+1}$. For conservation of tracer material during the regridding the following conditions must be satisfied:

$$T_{ij}^H(c_*^{H,h,n}) = T_{l,ij}^{\text{sum}}(c^{H,h,n}), \tag{23}$$

i.e. that the amount of tracer material in the coarse grid control volume $T_{ij}^H(c_*^{H,h,n})$ must be equal to the sum over the small grid control volumes of the original solution $T_{l,ij}^{\text{sum}}(c^{H,h,n})$. If we simply choose $c_*^{H,h,n} = c^{H,h,n}$ as in (22) condition (23) is not satisfied. If the midpoint rule is used, the integral approximation for the amount of tracer material in a control volume reads $T^H(c_*^{H,h,n}) = H_x H_y c_*^{H,h,n}$. Then, the value at the midpoint $c_*^{H,h,n}$ can be directly computed from condition (23) itself. The second cause for a change of the amount of tracer material during regridding occurs in regions where a fine grid is required at t_{n+1} but was not present at t_n. The data on the fine grid was provided by interpolation of the coarse grid data. The deficit in tracer material caused by the interpolation is given by

$$\Delta_{ij} = T_{ij}(c^{H,h,n}) - T_{l,ij}^{\text{sum}}(c_*^{H,h,n}). \tag{24}$$

In figure 12 we schematically represent this for a one-dimensional grid for the midpoint rule. We aim to correct the initial data for the new time step $c_*^{H,h,n}$ in such a way that the deficit is spread over all the fine grid points (x_{i+p}, y_{j+q}). The weights used for the distribution of the deficit in tracer material are given

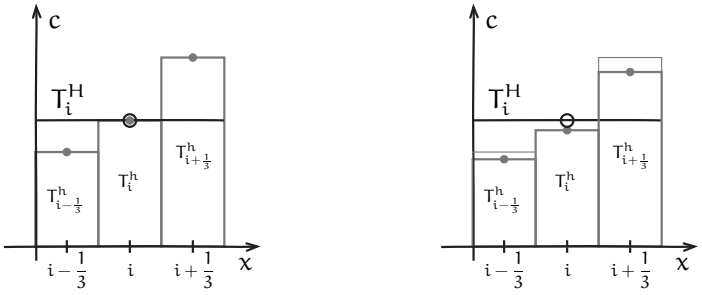

(a) after interpolation (b) correction for the tracer deficit

Fig. 12. Interpolating the coarse grid solution to provide the required data on new fine grid points. There is a deficit of tracer material introduced by the interpolation as the old amount of tracer material in the control volume T_i^H is not equal to the summed tracer material in the fine grid cells T^h (a). Distributing the deficit over the small grid cells leads to conservative regridding algorithm (b).

by

$$\alpha_{i+p,j+q} = \frac{T^h_{i+p,j+q}(c_*^{H,h,n})}{T^{\text{sum}}_{l,ij}(c_*^{H,h,n})} \tag{25}$$

Note that $\sum_{p,q} \alpha_{i+p,j+q} = 1$ which ensures that all the corrections summed over the fine grid points totals the deficit in tracer material Δ_{ij}. The updated solution

$$\bar{c}_*^{H,h,n}|_{(x_{i+p},y_{j+q})} = c_*^{H,h,n}|_{(x_{i+p},y_{j+q})} + \alpha_{i+p,j+q}\frac{\Delta_{ij}}{h_x h_y} \tag{26}$$

has the same amount of tracer material as the initial solution $T^H_{ij}(c^{H,h,n})$. The use of $\bar{c}_*^{H,h,n}$ as the initial data for the new time step, instead of c_*, ensures that tracer material is conserved.

A new simulation of the tracer dispersion during the dipole-wall collision is performed which uses the adapted defect and the conservative regridding algorithm. The relative error in the total amount of tracer material $|\mu(t)|$ is given in figure 13. Note that the use of the conservative regridding algorithm improves the conservation of tracer material by two orders of magnitude. The error in M is now $\mathcal{O}(10^{-6})$, a result that is reached using only one LDC iteration for each time step. A smaller error in the conservation of tracer material can be reached if more LDC iterations are performed.

7 Comparison between the LDC and spectral method

After comparing the standard and adapted definition for the local defect and making the regridding conservative, we are interested in how well the LDC method compares with standard spectral methods. Therefore, we use a spec-

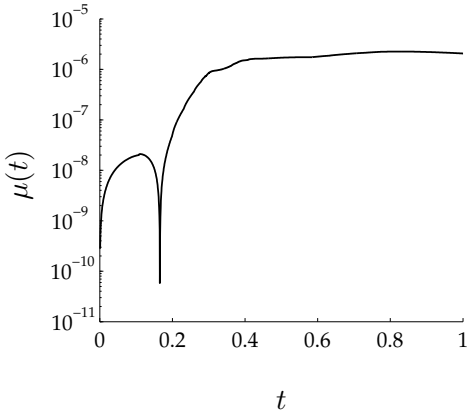

Fig. 13. The relative error $\mu(t) = |M(t) - M(0)|/M(0)$ in the total amount of tracer material for the adapted finite volume LDC method with conservative regridding.

tral method for solving the transport equation, which is based on the same expansion in Fourier and Chebyshev polynomials as used to calculate the velocity field [17]. In these simulations a resolution of $N = 768$ and $M = 768$ has been used for the tracer field, this is quite high as we want to have an accurate solution as benchmark data (see table 1). Note that the velocity for calculating the advection term in the transport equation is required at the same resolution, while it is only computed at the lower resolution 128×128 used to solve the Navier-Stokes equation. The increase in resolution is obtained by padding the matrix containing the spectral coefficients for the velocity with zeros to obtain the wanted resolution. After transforming this matrix to physical space, we obtain the velocity at a 768×768 grid. The time step used to solve the transport equation is $\Delta t_{\text{flow}} = 1.25 \times 10^{-5}$, such a time step is required for the stability of the time-discretization scheme (AB/CN) and will give accurate results. The used time step is equal to the one used to solve the velocity field, so there is no need to interpolate the data in time.

To asses how the finite volume method with the local defect correction method compares to the results of the spectral method we have plotted the contours of the passive tracer in figure 14. Between $t = 0.5$ and $t = 0.6$ the concentration varies most rapidly in time. There are only small differences visible between the LDC solution and the spectral solution. Note that the uniform grid size of the spectral method, which is approximately $2/768 = 2.6 \times 10^{-3}$, is comparable to the grid size at the finest LDC level $H_x/\sigma_x^2 = 2 \times 10^{-3}$. The smallest time step used on the finest grid, $\Delta t = 8 \times 10^{-6}$, is also comparable to the time step used to solve the flow and tracer transport with the spectral method, $\Delta t = 1.25 \times 10^{-5}$.

A more quantitative comparison can be made using integral quantities, like

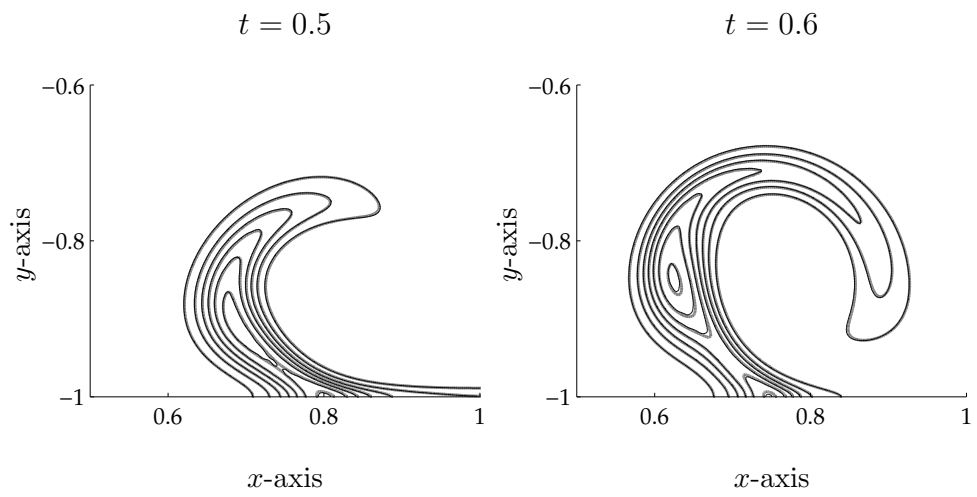

Fig. 14. Contour plots of the concentration computed by the LDC (black) and by the spectral method (grey) for $t = 0.5$ and $t = 0.6$.

the centre of mass of the tracer defined by

$$\overline{\mathbf{x}}(t) = \frac{1}{M}(\overline{x}(t), \overline{y}(t) = \int_{\Omega} \mathbf{x} c(\mathbf{x}, t) dA. \tag{27}$$

Note that this integral can be considered as a higher order moment of (21). Recall that we improved the algorithm for regridding to specifically satisfy conservation of tracer material. Therefore, it is interesting to investigate the error in higher order moments like the centre of mass and the variance in the tracer. The variance in the x-direction is given by

$$s_x(t)^2 = \frac{1}{M} \int_{\Omega} (x - \overline{x})^2 c(\mathbf{x}, t) dA, \tag{28}$$

a similar expression can be obtained for the variance in the y-direction. The relative differences for these quantities between the values obtained for the LDC and spectral simulations, *e.g.*

$$r_{\overline{y}}(t) = \left| \frac{\overline{y}_{\mathrm{LDC}}(t) - \overline{y}_{\mathrm{spectral}}(t)}{\overline{y}_{\mathrm{spectral}}(t)} \right|, \tag{29}$$

are plotted in figure 15. We left out the $\overline{x}$ as it constant in time due to the symmetry of the problem. For the spectral method the integral is computed by a sum over the spectral coefficients, which yields accurate results. The difference between $\overline{y}$ for the LDC and spectral method is somewhat smaller than 10^{-3}. The relative difference in variance is at most of order 3×10^{-3}. Note that the representation of the integrals is somewhat limited by the finite volume representation. The initial relative difference in the variance is already of order $\mathcal{O}(10^{-4})$.

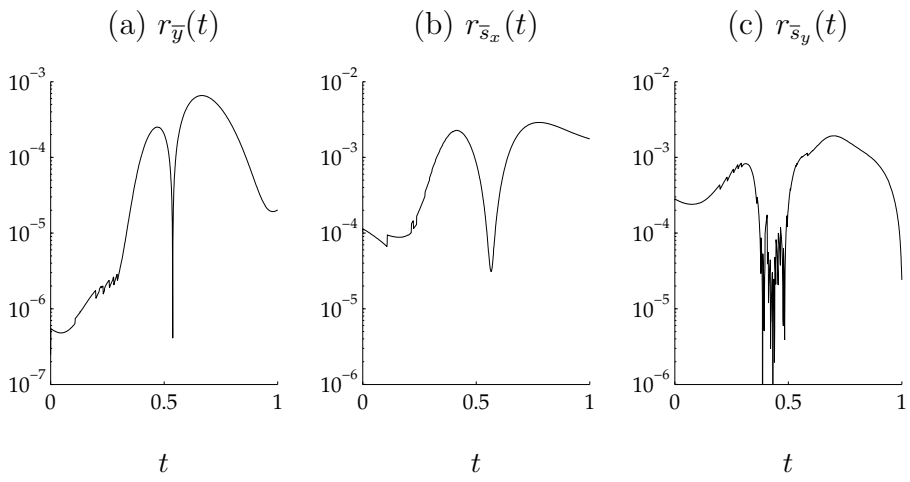

Fig. 15. The relative difference between the spectral and LDC solutions for (a) the centre of mass coordinate, (b) the variance in the x-direction and (c) the variance in the y-direction.

8 Conclusions

The local defect correction (LDC) algorithm provides a way to solve a transport problem for a localized tracer distribution on grids composed of uniform global and local grids. The idea behind LDC is to use the solution of the coarse global grid to provide the boundary condition to the local problems and then use the more accurate local solution to correct for the defect in the coarse global solution. In our case the solutions on global and local grids are computed using standard finite volume methods to solve the uniform grid problems. The correction to the defect can be adapted to ensure that tracer material conservation is satisfied on the composite of the global and local grids. However, simulations for a tracer blob advected in the velocity field of a dipole-wall collision reveal that there is some change in the amount of tracer material, a property that should be conserved. This change in the amount of tracer material is caused by the movement of the local fine grids, as the spatial interpolation of the data causes a deficit in tracer material. An straightforward method is applied to distribute the deficit over the grid points, which ensures the conservation of tracer material. Simulations performed with this kind of interpolation techniques give proper conservative results for the finite volume LDC method. The results for the conservative finite volume LDC method are compared to results obtained by a pseudo-spectral method. Concentration snapshots reveal a good agreement between both methods, only very small differences are visible. More quantitative comparisons are made for the integral quantities, centre of mass and variance of the tracer distribution. These show relative small differences between the LDC method and the spectral method.

We have shown that for the transport of a passive tracer the LDC method

can provide accurate results. The general idea behind LDC, to use the local fine grid to obtain an estimate for the defect on the global coarse grid, can be applied to other problems. Mass conservation for the composite solution can be reached by a slight change of the defect definition. In a way this illustrates the power of LDC, the coarse grid and fine grid solution are adapted to each other.

An interesting application of LDC is to use it for the computation of the velocity field itself. A clear application is to use such a method for the dipole-wall collision as the fine-scale dynamics remain restricted to a localized region. The simulation of turbulent flows remains outside the scope of LDC as fine-scale structures are not limited to a localized region. On the other hand, the initial dispersion of small blob of tracer material in the turbulent field can be computed using LDC.

9 Acknowledgments

Two of the authors (W.K. and R.M) were supported by the Computational Science programme (project 635.000.002) with financial aid from the Netherlands Organisation of Scientific Research (NWO).

References

[1] P. E. Dimotakis, Turbulent mixing, Ann Rev Fluid Mech 37 (2005) 329 – 356.

[2] B. Sawford, Turbulent relative dispersion, Ann Rev Fluid Mech 33 (2001) 289 – 317.

[3] Z. Warhaft, Passive scalars in turbulent flows, Ann Rev Fluid Mech 32 (2000) 203 – 240.

[4] R. A. Trompert, Local-uniform-grid refinement and transport in heterogeneous porous media, Adv Water Resour 16 (1993) 293 – 304.

[5] R. A. Trompert, J. G. Verwer, Analysis of the implicit Euler local uniform grid refinement method, SIAM J Sci Comput 14 (1993) 259–278.

[6] R. A. Trompert, J. G. Verwer, Runge-Kutta methods and local uniform grid refinement, Math Comp 60 (1993) 591 – 616.

[7] R. Minero, M. J. H. Anthonissen, R. M. M. Mattheij, A local defect correction technique for time-dependent problems, Numer Methods Partial Differential Eq 22 (2006) 128 – 144.

[8] R. Minero, M. J. H. Anthonissen, R. M. M. Mattheij, Solving parabolic problems using local defect correction in combination with the finite volume method, Numer Methods Partial Differential Eq 22 (2006) 1149–1172.

[9] R. Minero, H. G. ter Morsche, M. J. H. Anthonissen, Convergence properties of the local defect correction method for parabolic problems, Technical report CASA 05-40, Eindhoven University of Technology, Eindhoven (2005).

[10] P. Orlandi, Vortex dipole rebound from a wall, Phys Fluid A 2 (1990) 1429–1436.

[11] E. A. Coutsias, J. P. Lynov, Fundamental interactions of vortical structures with boundary layers in two-dimensional flows, Physica D 51 (1991) 482–497.

[12] H. J. H. Clercx, C.-H. Bruneau, The normal and oblique collision of a dipole with a no-slip boundary, Comput Fluids.

[13] R. Minero, Local defect correction for time-dependent problems, Ph.D. thesis, Eindhoven University of Technology (2006).

[14] B. A. V. Bennet, M. D. Smooke, Local rectangular refinement with application to nonreacting and reacting fluid flow problems, J Comp Phys 151 (1999) 684 – 727.

[15] B. A. V. Bennet, M. D. Smooke, Local rectangular refinement with application to axisymmetric laminar flames, Comb Theory Model 2 (1998) 221 – 258.

[16] B. A. Valdati, Solution-adaptive gridding methods with application to combustion problems, Ph.D. thesis, Yale University, New Haven, CT (1997).

[17] W. Kramer, Dispersion of passive tracers in two-dimensional bounded turbulence, Ph.D. thesis, Eindhoven University of Technology (2007).